Sunburned plankton: Ultraviolet radiation inhibition of phytoplankton photosynthesis in the Community Earth System Model version 2

Joshua Coupe^{1,2}, Nicole S. Lovenduski^{1,2}, Luise S. Gleason³, Michael N. Levy⁴, Kristen Krumhardt⁴, Keith Lindsay⁴, Charles Bardeen⁵, Clay Tabor⁶, Cheryl Harrison⁷, Kenneth G. MacLeod⁸, Siddhartha Mitra^{9,10}, and Julio Sepúlveda^{2,11}

Correspondence: Joshua Coupe (coupewx@gmail.com)

¹Department of Atmospheric and Oceanic Sciences, University of Colorado, Boulder, CO, USA

²Institute of Arctic and Alpine Research, University of Colorado, Boulder, CO, USA

³Department of Earth Science, University of California Santa Barbara, Santa Barbara, CA, USA

⁴Climate and Global Dynamics Laboratory, NSF National Center for Atmospheric Research, Boulder, CO, USA

⁵National Center for Atmospheric Research, Boulder, CO, USA

⁶Department of Earth Sciences, University of Connecticut, Groton, CT, USA

⁷Department of Oceanography & Coastal Sciences, Louisiana State University, Baton Rouge, LA, USA

⁸Department of Geological Sciences, University of Missouri, Columbia, MO, USA

⁹Department of Geological Sciences, East Carolina University, Greenville, NC, USA

¹⁰Virginia Institute of Marine Science, Gloucester Point, VA, USA

¹¹Department of Geological Sciences, University of Colorado, Boulder, CO, USA

Abstract. Ultraviolet (UV) radiation can damage DNA and kill cells. We use laboratory and observational studies of the harmful effect of UV radiation on marine photosynthesizers to inform the implementation of a UV radiation damage function for phytoplankton photosynthesis in a modified version of the Community Earth System Model version 2 (CESM2-UVphyto). CESM2-UVphyto is capable of simulating UV inhibition of photosynthesis among modelled phytoplankton and ocean column penetration of UV-A, UV-B, and UV-C radiation. We conduct a series of simulations with CESM2-UVphyto using the Marine Biogeochemistry Library (MARBL) ecosystem model to understand the sensitivity of phytoplankton productivity to UV radiation. Results from the simulations indicate that increased UV radiation shifts the vertical distribution of phytoplankton biomass and productivity deeper into the column, causes a moderate decline in total global productivity, and changes phytoplankton community structure. Our new CESM2-UVphyto model configuration can be used to quantify the potential ocean biogeochemical and ecosystem impacts resulting from events that disturb the stratospheric ozone layer, such as an asteroid impact, a volcanic eruption, a nuclear war, and stratospheric aerosol injection-based geoengineering.

1 Introduction

Marine phytoplankton, unicellular photosynthesizing microorganisms, are responsible for almost half of the primary production on Earth and as a result comprise the base of the marine food web (Falkowski, 2012). Phytoplankton photosynthesis and the associated drawdown of carbon dioxide are simulated in Earth system models with active ocean biogeochemistry and ecosystem components, which have been used to explore the response of global marine ecosystems to extreme events involving the injection of aerosols into the stratosphere (Lovenduski et al., 2020; Coupe et al., 2021; Harrison et al., 2022).

Photosynthesis requires light in a portion of the visible portion of the electromagnetic spectrum (400-700 nm wavelengths), i.e. photosynthetically active radiation (PAR). The relationship between phytoplankton photosynthesis and light is often represented by a photosynthesis-irradiance curve, where photosynthesis increases with light intensity until a specific threshold is reached at which point too much light can reduce phytoplankton photosynthetic capacity, also known as photoinhibition. This simplified formulation implicitly includes ultraviolet (UV, 280-400nm) inhibition, but does not consider an increasing ratio of UV radiation to PAR. At high absolute levels of UV radiation, photosynthetic apparatuses are damaged faster than repairs can be made (Cullen et al., 1992; Smith and Cullen, 1995), especially when PAR is low relative to UV. While UV inhibition of phytoplankton has been simulated in simple models (e.g., Cullen et al., 1992; Arrigo, 1994), most Earth system models do not explicitly include it.

Past work has used simple models to represent the biological effects of increased UV radiation on phytoplankton with biological weighting functions (BWFs) that quantify the relative cellular damage caused by UV radiation as a function of wavelength for different phytoplankton functional types (PFTs). BWFs were determined from laboratory studies where phytoplankton cultures were exposed to varying amounts of UV radiation. Photoinhibition effects are calculated by integrating the BWF over UV wavelengths and incorporating damage by UV radiation along with photoadaptation, which may counteract UV damage. When UV-B radiation is high and PAR is low, adaptation opportunities can become overwhelmed by UV damage. While phytoplankton-specific BWFs have been implemented in simple models to capture the response to increased UV

radiation (e.g., Arrigo, 1994), no coupled Earth system models currently include representation of UV radiation inhibition in marine phytoplankton. Yet, there are several potential use cases for Earth system models that incorporate UV inhibition of phytoplankton photosynthesis.

Short-lived events that deplete stratospheric ozone, such as large asteroid impacts, volcanic eruptions, or even nuclear war, may expose marine phytoplankton to harmful UV radiation by injecting aerosols and/or ozone depleting substances (ODS) into the stratosphere. One of the most well known asteroid impacts caused an extinction event at the Cretaceous-Paleogene boundary (K-Pg, ~66 million years ago) when the 10 km diameter Chicxulub asteroid struck the shallow sea near the present day Yucatan Peninsula (Alvarez et al., 1980; Smit and Hertogen, 1980; Schulte et al., 2010). Soot, dust, sulfur, carbon dioxide, water vapor, among other gases were emitted high into the atmosphere and likely caused an impact winter. While reduced sunlight and a sudden decline in temperature (Toon et al., 2016; Bardeen et al., 2017; Henehan et al., 2019; Tabor et al., 2020) were the primary drivers of extinction for a significant amount of marine and terrestrial organisms (Jablonski et al., 1997; Henehan et al., 2019; Tabor et al., 2020), the bombardment of the surface with UV radiation while life recovered from the impact winter may have slowed the return of photosynthesizers on land and in the ocean (Toon et al., 2016; Bardeen et al., 2017, 2021). Direct evidence of UV exposure following asteroid impacts can be challenging to identify due to the destructive nature of the cataclysmic events that may cause such anomalies. Paleoevidence of an increase in UV radiation contributing to an extinction event can be found in the form of malformed plant spores at the Carboniferous-Devonian boundary, lending some credibility to this mechanism (Marshall et al., 2020).

Model simulations allow for a quantification of ozone losses and associated increases in surface UV radiation. Simulations of a global nuclear war support the hypothesis that surface UV radiation would increase after an injection of soot aerosols into the stratosphere. Aerosol heating contributes to the decline of stratospheric ozone and increased surface UV-B radiation (280 to 315 nm) in the 6 to 9 years after the war even as PAR remains below average (Bardeen et al., 2021). Similar to nuclear war, asteroid impacts are likely to inject soot aerosols among dust, sulfates, and even halogens from vaporized seawater which could deplete ozone beyond the effects of warmer stratospheric temperatures. Model simulations of asteroid impacts over water show a decline in stratospheric ozone and increase in surface UV radiation, whether including soot, dust, and water vapor (Bardeen et al., 2021) or just water vapor and halogens (Pierazzo et al., 2010).

Aside from past and future hypothetical extinction-level events, there are several examples in recent history of stratospheric aerosol injection events disturbing the stratospheric ozone layer. Since 1970, several natural events have injected ODS into the stratosphere and caused transient declines in stratospheric ozone. The volcanic eruptions of El Chichón (1982) and Mt Pinatubo (1991) released sulfur dioxide, water vapor, hydrochloric acid, and hydrobromic acid into the atmosphere (Evan et al., 2023). After the Mt. Pinatubo eruption, the introduction of sulfate aerosols to the upper atmosphere caused warming in the stratosphere and accelerated the heterogeneous chemical reactions that deplete ozone. Surface cooling helped slowed the vertical and poleward transport of ozone rich air from the tropics, causing up to a 10% reduction in stratospheric ozone in the Northern Hemisphere mid-latitudes (Østerstrøm et al., 2023). In 2021, the Hunga Tonga submarine volcano eruption injected sulfates and an exceptional amount of water vapor (~50 Tg) into the stratosphere; a 5% decline in stratospheric ozone in the tropics followed (Vömel et al., 2022; Evan et al., 2023; Zhu et al., 2023). While most volcanic eruptions inject a plume of

predominantly sulfur dioxide in the stratosphere, the anomalous water vapor injection poses an additional risk for the ozone layer. Increased surface UV radiation from recent or potential future volcanic eruptions has been studied but possible ecosystem impacts as a result are understudied. Laboratory results of the estimated impact of ultraviolet radiation on phytoplankton shows there exists the potential for the ozone loss simulated in models of these volcanic eruptions to inhibit phytoplankton growth (Cullen et al., 1992). Similarly, the consequence of anthropogenic stratospheric aerosol emissions and its impacts on ocean ecosystems are also understudied.

75

80

85

100

Several "geoengineering" or climate intervention strategies have been proposed to either slow or reverse warming of the Earth's surface, but the evaluation of such actions aimed at the mitigation of climate hazards would benefit from better understanding their potential consequences for stratospheric ozone (Stratospheric aerosol injection; MacMartin et al., 2019; Tilmes et al., 2020). Deliberate injections of scattering aerosols into the stratosphere, which mimic the global cooling following volcanic eruptions that release sulfur, are likely to cause stratospheric warming and increase the heterogeneous chemical reactions that produce a depleted stratospheric ozone state (Tilmes et al., 2022). Deliberate sulfur based particle injections to reduce global mean surface temperatures were found to deepen the Antarctic ozone hole within 10 years using a high-top version of the Community Earth System Model (CESM) with interactive stratospheric chemistry (Tilmes et al., 2021). While little is known about the biological impacts of these climate intervention strategies, we can look to the past for an example of anthropogenic emission of an ODS that has been studied for its effects on marine ecosystems.

The multi-decadal increase in atmospheric chlorofluorocarbon (CFC) concentrations was responsible for the formation of the Antarctic ozone hole (Solomon et al., 1986), which increased surface UV radiation as far north as Australia and spurred significant scientific research into the biological effects of UV radiation. The global ban on manufacturing of CFCs via the Montreal Protocol in 1987 halted emissions to near zero, slowing the growth of the ozone hole in the following decades (Garcia et al., 2012). Though this destruction and recovery of stratospheric ozone likely had significant biological impacts, the lack of observational studies documenting temporal trends among marine phytoplankton limits scientists' ability to understand the biological response of this community as a function of changing UV irradiance (Smith and Cullen, 1995). In lieu of observational studies, lab grown phytoplankton can be exposed to varying levels of UV radiation to quantify their sensitivity to something like an ozone hole (Cullen et al., 1992).

Finally, marine phytoplankton exposure to UV radiation may increase in some regions as anthropogenic climate change warms the Earth's surface, representing a compounding threat. The warming of the Earth's surface in regions where wind speeds do not increase may increase the density gradient in the upper ocean (Li et al., 2020), resulting in increased stratification that concentrates phytoplankton in the surface layers of the ocean where these organisms are exposed to higher amounts of harmful UV radiation (Gao et al., 2019). Mineralizing phytoplankton, such as diatoms (silica frustules) and coccolithophores (calcium carbonate shells) rely on their shell-like structures for physical protection, but the production of these shells may be disrupted by UV radiation (Neale et al., 1998; Lorenzo et al., 2019). Coccolithophore shells, also known as coccospheres, play a role in filtering damaging UV light (Xu et al., 2016), but may thin in response to ocean acidification (Ridgwell et al., 2009; Fox et al., 2020; Krumhardt et al., 2019). Diatom frustules offer similar protection from UV radiation, but in contrast

to coccospheres, these silica-based structures dissolve more slowly in an acidified ocean (Aguirre et al., 2018; Taucher et al., 2022).

Numerous potential use cases motivate our development of an Earth system model capable of simulating phytoplankton photosynthesis inhibition by UV radiation. Here, we describe the implementation of this new capability in the Community Earth System Model version 2. We test the new model formulation using simulations with varying levels of UV radiation. As we will demonstrate, UV radiation perturbs the vertical distribution of phytoplankton biomass and productivity while causing moderate decline in global phytoplankton productivity and changes in phytoplankton community structure. Our new model addition is a useful tool for exploring both natural and anthropogenic events that may increase marine phytoplankton exposure to UV radiation.

2 Materials and Methods

2.1 Model Components

120

125

130

135

We use the Community Earth System Model version 2.1.5 (CESM2) with atmosphere, ocean, sea ice, and land components that exchange information with each other through a coupler (Danabasoglu et al., 2020). Our modifications produce a model that is capable of simulating UV radiation in the atmosphere and propagating it through the ocean column, where it inhibits phytoplankton photosynthesis. We call our modified model version CESM2-UVphyto.

The atmospheric model used for this study is the Whole Atmosphere Community Climate model version 4 (WACCM4, Marsh et al., 2013), using a grid with 1.9 x 2.5 degree horizontal resolution, 66 vertical layers and a 140 km model top. WACCM4 model includes a mathematical representation of stratospheric circulation, thermodynamics, and chemistry, the last of which is crucial for simulating UV radiation. As a "high top" model it can resolve the stratosphere in addition to parts of the mesosphere. The Tropospheric Ultraviolet and Visible (TUV) model version 4.2 (Zerefos and Bais, 1997) is added to WACCM4, as Bardeen et al. (2021) did, and calculates spectral integrals in-line across 100 wavelength intervals between 120 and 750 nm, instead of using a look-up table approach. Radiation between 121 nm and 400 nm from TUV is used to compute biologically relevant parameters. The Rapid Radiative Transfer Model for GCMs (RRTMG; Iacono et al., 2000) is used for atmospheric radiative transfer not within the UV range.

WACCM4 includes the chemistry modifications described in Bardeen et al. (2021) and a module to inject stratospheric soot and ozone-depleting halogens, specifically hydrogen bromide and hydrogen chloride. TUV is modified to allow actinic flux to be affected by the optical effects of aerosols. Biological weighting functions that determine UV inhibition of phytoplankton photosynthesis are also incorporated into TUV (Zerefos and Bais, 1997; Bardeen et al., 2021), which also calculates surface UV-A, UV-B, and some UV-C radiation. UV-A radiation is between 320 nm and 400 nm, UV-B radiation is between 280 nm and 320 nm, and UV-C radiation is defined as 100 nm to 280 nm but the model is only able to compute spectral integrals from 121 to 280 nm. The spectrally integrated biological weighting functions are computed explicitly over UV-B and UV-A radiation and sent to the coupler and then to the ocean at hourly frequency, identical to the treatment of shortwave radiation by RRTMG.

The ocean model component is the Parallel Ocean Program version 2 (POP2; Danabasoglu et al., 2020). POP2 has a nominal horizontal resolution of 1 degree with 60 vertical levels, with a uniform vertical resolution of 10 m in the upper 150 m, which increases to a maximum vertical spacing of 250 m between 3500 m and its maximum depth of 5500 m. POP2 is coupled to an ocean biogechemistry and ecosystem model called the Marine Biogeochemistry Library (MARBL), which has the flexibility to resolve different plankton configurations (MARBL; Long et al., 2021). The version of MARBL used here includes four phytoplankton functional types (PFTs), small phytoplankton, diatoms, diazotrophs, and coccolithophores, and two zooplankton functional types (microzooplankton and mesozooplankton), a configuration referred to as "4p2z" (Krumhardt et al., 2024). MARBL-4p2z simulates multiple nutrient co-limitation for all four PFTs.

In MARBL, small phytoplankton are limited by nitrogen, phosphorus, and iron. The small phytoplankton functional group represents a diverse group of phytoplankton, from *Prochlorococcus* and *Synechococcus* in warm, oligotrophic regions to groups like *Phaeocystis*, cryptophytes, and picoeukaryotes in upwelling or polar regions. Because of the diversity of the phytoplankton contained within the small phytoplankton functional group, phytoplankton in high latitude regions that are often highly temperature and light limited may not be as well represented in this model. Diazotrophs are nitrogen fixing bacteria that are limited by phosphorus and iron. Diatoms are silicifiers that are limited by nitrogen, phosphorus, iron, and are the only PFT limited by silicon. Coccolithophores are limited by nitrogen, phosphorus, iron, and are the only PFT limited by carbon. The coccolithophore PFT is primarily represented as *Emiliania huxleyi* in MARBL-4p2z, based on Krumhardt et al. (2019), and simulates calcium carbonate production as a function of temperature, aqueous CO₂, and phosphorus limitation. In total, the dynamics of four morphotypes of *Emiliania huxleyi*, as well as other species such as *Calcidiscus leptoporus* and *Gephyrocapsa oceania* were used to construct the PFT, allowing the model to simulate the general response of coccolithophores to environmental changes Krumhardt et al. (2019). Microzooplankton graze on phytoplankton, while mesozooplankton graze on both phytoplankton and microzooplankton. Other than grazing, loss of phytoplankton can occur through aggregation and subsequent sinking through the column.

Phytoplankton photosynthesis in all MARBL configurations is calculated by scaling the maximum growth rate by limitation functions for temperature, light, and nutrient availability (Long et al., 2021). Phytoplankton photosynthesis increases in response to increasing PAR, following the light limitation formulation from Geider et al. (1998). Photoadaptation is represented as a varying chlorophyll to carbon ratio for each PFT, depending on light, temperature, and nutrient limitations (Geider et al., 1998). PAR in MARBL is estimated as 45% of surface shortwave radiation and is attenuated with depth as a function of chlorophyll concentration, taking into consideration shading by phytoplankton. Zooplankton are not considered in the light attenuation equation, as they do not contain chlorophyll and do not absorb light as effectively as phytoplankton. In high concentrations, zooplankton may impact light attenuation, but these populations tend to overlap with high phytoplankton concentrations which already significantly attenuate light. In CESM2-UVphyto, phytoplankton growth rates can be slowed by increased UV radiation, as described in Section 2.2. While TUV provides a direct calculation of PAR, the simulations here use the PAR estimation from shortwave radiation in order to test the sensitivity of the model to the new UV radiation scheme alone.

Source code modifications to WACCM4, TUV, POP2, and MARBL were required to enable the calculation of UV inhibition. In WACCM4, this includes the integration of TUV and modules used to simulate aerosol injections relevant for asteroid impacts (Bardeen et al., 2017, 2021). New BWFs relevant for the phytoplankton species simulated in MARBL were added to TUV. Modifications to the CESM2 model coupler were made to pass UV radiation fields to POP2, and POP2 was modified to pass information to MARBL, where UV inhibition of photosynthesis is calculated. All other components are used without modification from the cesm2.1.5.

The sea ice model is CICE5 with interactive sea ice that shares the same horizontal grid as POP2 (Hunke et al., 2015). CICE5 includes mushy-layer thermodynamics and a melt pond parameterization that produces melt ponds preferentially on undeformed sea ice. Sea ice is allowed to affect PAR attenuation with depth in the ocean model using a subgrid-scale sea ice thickness distribution (Long et al., 2015). Essentially, various sea ice thickness categories can impact the ability of phytoplankton to grow underneath sea ice. In CESM2-UVphyo, UV radiation interaction with sea ice is identical to the treatment of shortwave radiation, until UV radiation reaches the water, at which point its attenuation accelerates rapidly compared to PAR.

The land model is the Community Land Model version 5 (CLM5) with a carbon-nitrogen cycle (Lawrence et al., 2019). It simulates the evolution of the land physical state, characteristics of the land surface, exchanges of energy and material with the atmosphere, and run-off into the ocean. CLM5 has a horizontal resolution of 1.9 x 2.5 degrees which is shared with the atmosphere grid, with 15 vertical layers for the land and 10 vertical layers for lakes. Photosynthesis of terrestrial vegetation is not inhibited by UV radiation, but future work is expected to incorporate this functionality.

2.2 Calculation of Ultraviolet Inhibition of Photosynthesis

180

185

190

200

Biological weighting functions (BWF) for UV inhibition for each PFT (see Section 2.3) are integrated over the UV-A, UV-B, and UV-C portions of the electromagnetic spectrum in TUV and used to calculate surface E_{inh}^* , a biologically weighted dimensionless UV dosage rate, according to Cullen et al. (1992),

$$E_{inh}^* = \sum_{\lambda=200nm}^{400} E(\lambda) \cdot \epsilon(\lambda) \cdot \Delta\lambda, \tag{1}$$

where $E(\lambda)$ is the surface spectral irradiance at wavelength λ , and $\epsilon(\lambda)$ is the BWF ((mW m²) $^{-1}$) representing the inhibition of photosynthesis by UV radiation. λ spans the UV spectrum of radiation from 121 nm to 400 nm and is subdivided into UV-A, UV-B, and UV-C components. E^*_{inh} can be thought of as the total integrated potential damage phytoplankton will suffer from radiation in the UV spectrum. While some laboratory studies include a PAR inhibition term in E^*_{inh} (Neale and Thomas, 2016), our model configuration does not account for this term; in our simulations, high UV is not accompanied by high PAR. The BWF, given by $\epsilon(\lambda)$, describes how each wavelength interval contributes to that damage. E^*_{inh} values are determined at every surface model grid cell and time step for small phytoplankton, diatoms, diazotrophs, and coccolithophores.

 E_{inh}^* is passed from the atmospheric model (TUV) to the marine biogeochemistry model (MARBL) and propagated vertically through the water column. To capture the rapid attenuation of UV radiation with depth in the ocean, we compute E_{inh}^* at a given model level using the relationship between chlorophyll and the attenuation coefficient ($K_{d,UV}$) in Tedetti et al. (2007).

Because attenuation varies as a function of wavelength, E_{inh}^* is subdivided into UV-A, UV-B, and UV-C components before being passed to the ocean. The attenuation coefficient, $K_{d,UV}$ has three forms: $K_{d,UV-A}$, $K_{d,UV-B}$, or $K_{d,UV-C}$, calculated using the following relationships where the attenuation coefficient is computed as a function of chlorophyll (CHL, mg m⁻³):

205
$$K_{d,UV-A} = 0.24 \cdot \text{CHL} + 0.04,$$
 (2)

$$K_{d,UV-B} = 0.44 \cdot \text{CHL} + 0.13,$$
 (3)

$$K_{d,UV-C} = 0.60 \cdot \text{CHL} + 0.40,$$
 (4)

This is based on an equation that was determined empirically under open ocean conditions (Tedetti et al., 2007). E_{inh}^* is propagated through the column as a function of K_{d-UV} and the thickness of a particular model layer, dz (m):

$$E_{inh}^*(k+1) = E_{inh}^*(k) \cdot exp(-K_{d,UV} \cdot dz), \tag{5}$$

where k is the vertical layer index. According to this relationship, for chlorophyll concentrations of 0.02 mg m⁻³ (the minimum value used for calculating the impact of chlorophyll on the vertical propagation of PAR in MARBL), the depth at which UV-B radiation declines to 1% of its surface value ($Z_{1\%}$) is ~33 m. At higher chlorophyll concentrations (~0.85 mg m⁻³) $Z_{1\%}$ for UV-B radiation is ~9 m depth, effectively restricting UV inhibition to the first model level. In the clearest waters possible, $Z_{1\%}$ of UV-C radiation is 11 m, while at chlorophyll concentrations of 0.85 mg m⁻³, $Z_{1\%}$ for UV-C radiation is approximately 5 m, or the midpoint of the first model level. UV-A radiation propagates to ~98 m depth before reaching $Z_{1\%}$ under the clearest waters, indicating greater potential for UV-A damage than for UV-B and UV-C. We use the mid-point of the layer to calculate attenuation for each layer, which may underestimate the influence of much higher E_{inh}^* within the top 5 m of the level, but could overestimate E_{inh}^* within the bottom 5 m of the level. The effect of ocean surface roughness from waves on UV radiation entering the surface ocean is not considered in the attenuation of UV radiation.

220

225

Finally, a UV inhibition term (γ_{UV}) is computed at every model level, similar to nutrient and light limitation. γ_{UV} is computed using three different functional forms or "models", depending on the functional form used to derive the biological weighting functions (Table 1). These include the "E" model, the "T" model, and the "Emax" model, which relate E_{inh}^* to γ_{UV} . γ_{UV} ranges from 0 (total UV inhibition) to 1 (no UV inhibition) and is included in the calculation of the growth rate for phytoplankton from Long et al. (2021),

$$\mu_i = \mu_{max}(T) \cdot \gamma_N \cdot \gamma_l \cdot \gamma_{UV},\tag{6}$$

where μ_i represents the growth rate of a particular PFT, $\mu_{max}(T)$ represents the maximum growth rate at a given temperature, and γ_N and γ_l represent nutrient and light limitation terms, respectively, ranging from 0 (no nutrients/light) to 1 (sufficient nutrients/light). In this way the γ limitation terms reduce the maximum growth rate multiplicatively.

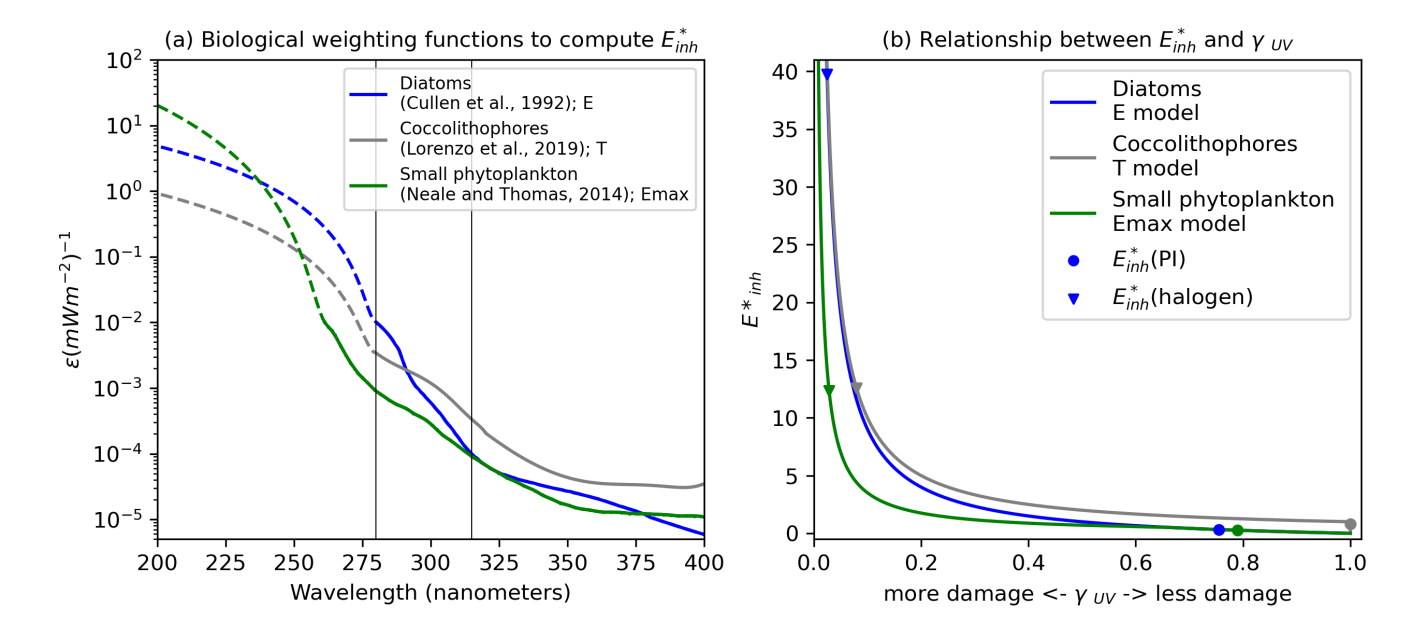


Figure 1. (a) Species-specific biological weighting functions showing the biological efficiency for inhibition of phytoplankton photosynthesis by ultraviolet light as a function of wavelength. Depicted here are the weighting functions for diatoms (Cullen et al., 1992), coccolithophores (Lorenzo et al., 2019), small phytoplankton and diazotrophs (Neale et al., 2014) that were used in simulations of CESM2-UV. Dashed lines indicate extrapolated values and the vertical black lines are the divisions of UV-C/UV-B and UV-B/UV-A radiation from left to right. (b) Relationship between E_{inh}^* and γ_{UV} for the different phytoplankton functional types and models and under different UV conditions.

2.3 Determination of Biological Weighting Functions

235

240

245

The expansion of the Southern Hemisphere ozone hole during the 1980s due to the emission of chlorofluorocarbons in the decades prior prompted studies into the susceptibility of marine life and phytoplankton to UV radiation. These efforts produced biological weighting functions (BWFs) specific to different PFTs that are suitable for the simulation of UV inhibition of photosynthesis. We utilized both laboratory and *in-situ* studies with appropriate BWFs for the phytoplankton community represented within MARBL (Figure 1). For diatoms, we used the BWF based on the E model reported in Cullen et al. (1992), who measured changes in productivity of the diatom *Phaeodactylum sp.* by exposing samples of the species to a range of wavelengths of UV and PAR. Look-up tables are provided as csv files in *Model code and software* for the three BWFs shown in Figure 1a. Wavelengths are interpolated to the bounds provided in this table to calculate spectral integrals. Diatoms show relatively low sensitivity to UV-A light, but are exponentially more sensitive to UV-B light, especially for wavelengths shorter than 290 nm.

For coccolithophores, we adopted the BWF reported for a heavily calcified species of *Emiliana huxleyi* by Lorenzo et al. (2019) which was constructed using the T model (see Table 1.). The T model permits no UV limitation until E_{inh}^* reaches 1, at which point damage is more sensitive to changes in radiation than in the E model. Because laboratory experiments have

Table 1. Different phytoplankton functional types (PFTs) and the study that determined the specific biological weighting functions (BWFs) we used in simulations of CESM2-UVphyto. Units are in $(mW m^{-2})^{-1}$.

| Phytoplankton | Study | Equation | |
|---|----------------------------|--|------|
| Siliceous Diatoms | Cullen et al. (1992) | E model $\gamma_{UV} = \frac{1}{1 + E^*_{inh}},$ | (7) |
| Calcifying Coccolithophores | Lorenzo et al. (2019) | T model $\gamma_{UV} = 1, E^*_{inh} < 1$ | (8) |
| | | $\gamma_{UV} = \frac{1}{E_{inh}^*}, E_{inh}^* \ge 1$ | (9) |
| Small phyto- plankton and Diazotrophs | Neale and Thomas (2014) | Emax model $\gamma_{UV} = \frac{1}{1 + E^*_{inh}}, E^*_{inh} \leq E^*_{max}$ | (10) |
| | | $\gamma_{UV} = \frac{1}{C * E_{inh}^*}, E_{inh}^* > E_{max}^*$ | (11) |
| | | $c = \frac{1 + E_{max}^*}{E_{max}^*};$ | (12) |
| | | $E_{max}^* = 0.54$ | (13) |
| | | | |

revealed that the thinning of coccolithophore shells may make them more susceptible to UV damage (e.g. Guan and Gao, 2010), our model includes an optional feature that enhances UV damage when environmental conditions result in thinned coccolithophore shells (thickness determined by the PIC/POC ratio; see Section 2.4).

We use the *Synechococcus* BWF reported in Neale et al. (2014) for both small phytoplankton and diazotrophs. Neale et al. (2014) and Neale and Thomas (2016) studied UV sensitivity of *Prochlorococcus* and *Synechococcus* from temperate and tropical open-ocean regions under different UV exposures and water temperatures. The BWF for *Synechococcus* from Neale

et al. (2014) most closely resembles the species that the small phytoplankton functional group in MARBL is intended to represent. This BWF is constructed using the Emax model, which is equivalent to the E model until E_{inh}^* surpasses 0.54, at which point UV damage increases as a much faster rate as E_{inh}^* increases.

The effects of UV radiation on diazotrophs have been examined to some extent (Lesser, 2008; Cai et al., 2017), but none have reported usable BWFs for computing UV damage as a function of wavelength. Lesser (2008) found that diazotrophs were quite sensitive to UV radiation, while Cai et al. (2017) found that UV-absorbing compounds in high-light grown diazotrophs (*Trichodesmium*) can mitigate some but not all UV damage. The shallow depth of *Trichodesmium* coupled with its importance of supplying nitrogen to oligotrophic gyre ecosystems suggests a potentially important regional role for UV inhibition of nitrogen fixers. We generalize diazotrophs by using the same BWF as reported by Neale et al. (2014), therefore representing a mid-point between the BWFs for the diatoms and coccolithophores. Diazotrophs lack mineral shells like diatoms and coccolithophores, and thus are more akin to small phytoplankton in their sensitivity to UV. Diazotrophs comprise less than 3% of global phytoplankton net primary productivity in pre-industrial MARBL-3p1z simulations, meaning large uncertainties in how diazotrophs will respond to UV radiation do not significantly affect global productivity or nutrient cycling over shorter (decadal) timescales but may have regional impacts that CESM2-UVphyto can consider.

Not all of the employed BWFs extend into wavelengths below 280 nm (UV-C radiation). While UV-C radiation is a non-factor even under a relatively depleted ozone layer, it may become relevant after a cataclysmic asteroid impact. We account for potential UV-C radiation damage by extrapolating the BWFs to wavelengths of 200 nm (dashed lines in Figure 1a).

2.4 Scaling UV inhibition of coccolithophore photosynthesis as a function of shell thickness

255

260

265

Coccolithophores construct shells out of calcium carbonate, providing protection from grazing, viral attacks, as well as from harmful amounts of PAR and UV radiation (Monteiro et al., 2016; Krumhardt et al., 2019; Xu et al., 2016; Lorenzo et al., 2019). In MARBL, coccolithophores have the lowest maximum grazing rate, partly because of the protection from their shell. Laboratory studies of calcified and thin-shelled, or "naked" coccolithophores have found that the shell reduces the transmission of UV-B radiation by 18% (Xu et al., 2016). In response to decreased transmission of UV-B, calcified cells in outdoor conditions were also found to have 3.5 times higher growth rates than "naked" coccolithophores (Xu et al., 2016). When UV was removed in indoor conditions, growth rates were still 2 times higher than in outdoor conditions, indicating a growth enhancement of 1.75 times when UV is not present.

In CESM2-UVphyto, coccolithophore shell thickness is related to the instantaneous ratio of particulate inorganic carbon (PIC; calcium carbonate) to particulate organic carbon (POC), $\frac{PIC}{POC}$ (Krumhardt et al., 2019). Shelled coccolithophores have a $\frac{PIC}{POC}$ > 0.05, while 'naked' coccolithophores have a $\frac{PIC}{POC}$ <=0.05. In CESM2, PIC/POC is also influenced by the aqueous CO₂ concentration, such that elevated CO₂ corresponds with lower PIC/POC values (Krumhardt et al., 2019). To accommodate the UV inhibition of coccolithophore photosynthesis that accompanies thinning coccolithophore shells, we have included a PIC/POC scaling option that can be toggled on and off, where we modify γ_{UV} when a minimum level of UV damage is reached (E_{inh}^*) > 0.25) as follows:

 $\gamma_{UV}(\text{shelled}) = S \cdot \gamma_{UV}(\text{naked}), \tag{14}$

where

295

300

$$S = \begin{cases} 1.75^{-1}, & \text{if } \frac{PIC}{POC} < 0.05, \\ \left(\frac{PIC}{POC}\right)^{\frac{1}{6}}, & \text{otherwise.} \end{cases}$$
 (15)

Our γ_{UV} scaling aligns with the Xu et al. (2016) finding that calcified cells have growth rates 3.5 times higher than naked shells under moderate levels of UV radiation. As CESM2-UVphyto does not have explicit PAR inhibition, we adjust the scaling factor downwards to 1.75.

2.5 Pre-industrial simulations with low UV radiation

We conduct two simulations with CESM2-UVphyto under no or low levels of UV radiation to ensure that our new BWFs do not disrupt the normal functioning of the biogeochemical and ecosystem model. Both of these test simulations use the 4p2z configuration of MARBL and pre-industrial atmospheric forcing consistent with the year 1850 and atmospheric CO₂ concentration set to 284.7 ppm. The first is a 10-year coupled simulation of CESM2-UVphyto with an E_{inh}^* value of zero that branches from a previously spun-up ocean physical and biogeochemical state (Krumhardt et al., 2024); the UV forcing from this simulation is referred to as $E^*_{inh}(0)$. The end of the $E^*_{inh}(0)$ simulation is used as the initial condition for all subsequent simulations. The second simulation probes the impact of the new BWFs on the resulting biogeochemical state under 5 years of pre-industrial (i.e., low) UV radiation levels, $E_{inh}^*(PI)$. This simulation of ocean biogeochemical sensitivity to pre-industrial levels of UV radiation (and subsequent ones) are conducted in ocean-ice only mode, i.e., a simulation of CESM2-UVphyto with only the ocean and ice component models that is forced by saved surface states and fluxes from coupler output files; UV-A, UV-B, and UV-C radiation; and E_{inh}^* for each BWF at the air-sea interface. These forcings are derived from a year-long, fully coupled simulation of CESM2-UV phyto with WACCM4 coupled to TUV under pre-industrial levels of UV radiation, and produce a global average annual mean surface E_{inh}^* (diatoms) of 0.32, E_{inh}^* (small phytoplankton & diazotrophs) of 0.82, and E_{inh}^* (coccolithophores) of 0.27. Because of the lack of ODS in the pre-industrial stratosphere, UV radiation is elevated in the present day compared to the pre-industrial in terms of UV index by up to 13% in tropical regions, 10% in the Antarctic, and 4% in Arctic regions. However, the surface UV radiation levels present in these simulations are well within the range of those used in laboratory studies that informed the construction of BWFs.

2.6 Pre-industrial simulations with elevated UV radiation

We conduct 5 year simulations to explore the modeled biogeochemical and ecological response to high levels of surface UV radiation. Halogens equivalent to emissions from the Chicxulub asteroid impact at the K-Pg boundary Toon et al. (2016) are injected into the stratosphere. The halogen injection includes 117,000 Tg hydrogen chloride and hydrogen bromide and

is intended to mimic an upper bound of a possible surface UV radiation perturbation without affecting visible light. Global atmospheric circulation is affected by the depletion of stratospheric ozone, but there are minimal changes to the surface radiative budget. This case is referred to as E_{inh}^* (halogen). A fully coupled simulation is run for two years and coupler forcing is used to generate a five-year offline simulation; for simplicity, the forcing from the second year of the fully coupled simulation is repeated for 4 years for the offline simulation.

2.7 Elevated CO₂ simulations

315

320

At higher atmospheric CO₂ concentrations, coccolithophores in some regions may experience a carbon fertilization effect as carbon used for photosynthesis become less limiting, allowing for faster growth compared to lower CO₂ concentrations (Krumhardt et al., 2017, 2019). However, coccolithophores' ability to construct and maintain thick calcium carbonate shells (i.e., high PIC/POC ratios) may be inhibited (Krumhardt et al., 2019). To explore UV inhibition in conditions that engender thinner coccolithophore shells, we conducted a range of ocean and sea-ice only simulations with varying atmospheric CO₂ concentrations at the ocean's surface: 284 ppm, 400 ppm, 600 ppm, 700 ppm, and 900 ppm. First, these simulations are spunup with no UV radiation inhibition ($E_{inh}^*(0)$) and CO_2 = 284.7 ppm until the mixed layer (0-100m) global average pH exhibits little change with time, occurring after 15 years of simulation. The simulation with $CO_2 = 400$ ppm uses the end of the $CO_2 = 400$ ppm uses the end of $CO_2 = 400$ pp 284 ppm simulation as an initial condition, the end of the simulation with CO₂= 400 ppm is used as the initial condition for the 600 ppm simulation, the end of the simulation with CO_2 =600 ppm is used to start the 700 ppm simulation, and the end of the simulation with CO₂=700 ppm is used to start the 900 ppm simulation. This approach speeds up the spin-up as atmospheric CO₂ concentrations progress higher. All simulations with CO₂ levels greater than 284.7 ppm are run for 17 years, at which point variations in upper ocean global average pH are smaller than 0.01 from year to year. Next, $E_{inh}^*(PI)$ is imposed for 1 year starting at the end of each simulation with incrementally increasing atmospheric CO₂ (400 ppm, 600 ppm, 700 ppm, 900 ppm). Finally, E_{inh}^* (halogen) is imposed for 1 year in the same manner as E_{inh}^* (PI), using the same initial condition. Detailed information about each simulation can be found in Table S1.

335 3 Results

340

UV radiation at the ocean's surface causes a reduction in globally integrated phytoplankton net primary productivity (NPP) through inhibition of photosynthesis in the top 40 m of the ocean under $E^*_{inh}(\text{PI})$ and $E^*_{inh}(\text{halogen})$ forcing. Under the control $E^*_{inh}(0)$ forcing, annual-mean globally integrated top 150 m NPP equilibrates to 55 Pg C yr $^{-1}$ in the 4p2z configuration, which is well within the range of satellite estimates (43-67 Pg C yr $^{-1}$; Behrenfeld and Falkowski, 1997 and Behrenfeld et al., 2006) and similar to other configurations of MARBL (Long et al., 2021). Under $E^*_{inh}(\text{PI})$ UV forcing, annual-mean global NPP is reduced by 5.4% compared to $E^*_{inh}(0)$, as shown in Figure 2a. The results indicate a statistically significant change in global NPP under pre-industrial UV radiation compared to simulations without UV radiation. In the $E^*_{inh}(\text{halogen})$ case, annual-mean globally integrated NPP declines by 6.5% to 51.9 Pg C yr $^{-1}$ compared to the $E^*_{inh}(0)$ simulation (Figure 2a). Under

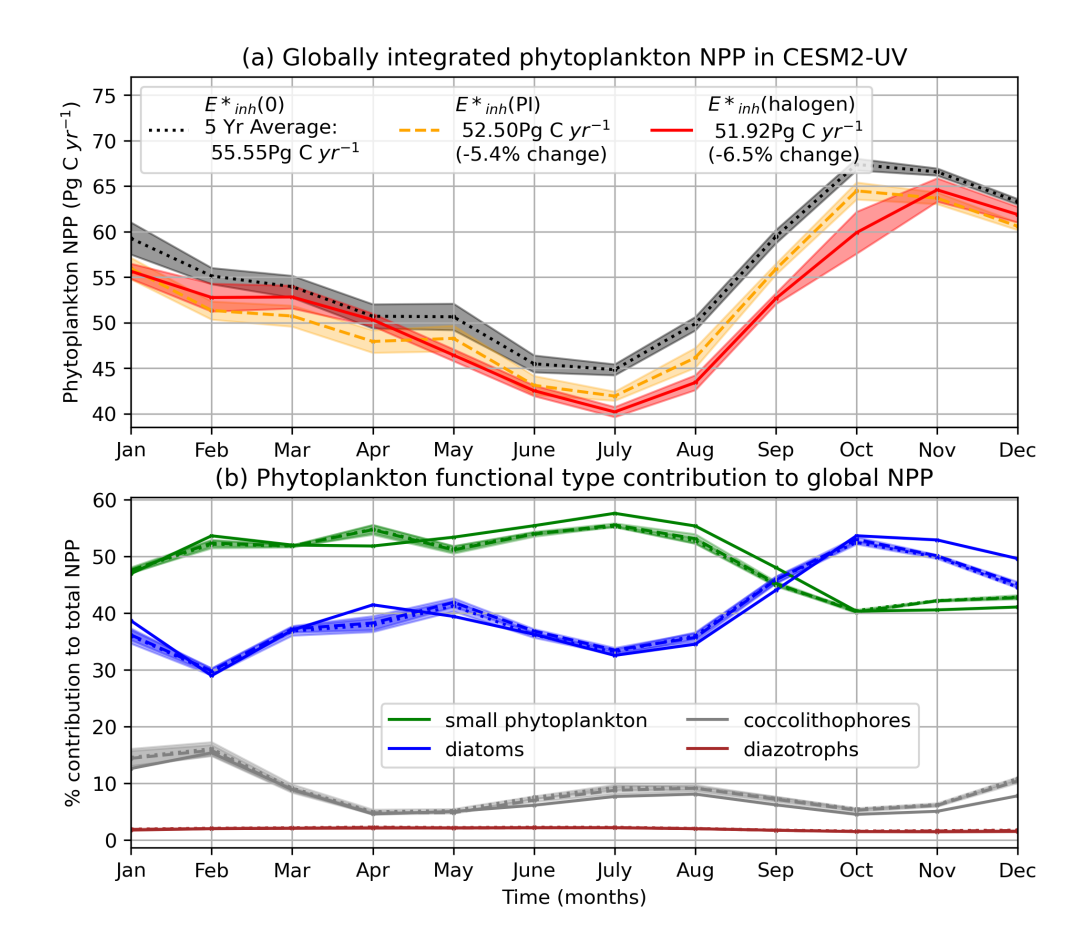


Figure 2. (a) Globally integrated 5-year mean monthly NPP climatology integrated over the top 150 m (Pg C yr^{-1}) in the $E^*_{inh}(0)$, $E^*_{inh}(PI)$, and $E^*_{inh}(halogen)$ simulations. Shading indicates 1 standard deviation below and above the 5-year mean for each month. (b) Each phytoplankton functional type's % contribution to globally-integrated NPP in the (solid) $E^*_{inh}(halogen)$, (dashed) $E^*_{inh}(PI)$, and (dotted) $E^*_{inh}(0)$ simulations. Note the $E^*_{inh}(PI)$ and $E^*_{inh}(0)$ simulations are nearly indistinguishable.

 E_{inh}^* (halogen), stratospheric ozone declines by more than 90%, producing UV indices greater than 30 over the Antarctic, exceeding the greatest values of up to 14 over Antarctica under the ozone hole.

345

The phytoplankton productivity response to UV inhibition is a function of characteristics unique to each phytoplankton type, with some types benefiting at the expense of others. Small phytoplankton constitute half of the annual mean globally integrated NPP in both the $E_{inh}^*(0)$ and $E_{inh}^*(PI)$ simulations (Figure 2b), while diatoms contribute approximately 40%. Together, both coccolithophores and diazotrophs contribute around 10% to global NPP. Under preindustrial levels of UV radiation (case $E_{inh}^*(PI)$), the relative contribution of each PFT to global NPP is virtually unchanged and the timing of seasonal blooms are not significantly altered when compared to the $E_{inh}^*(0)$ case (Figure 2b). Under $E_{inh}^*(halogen)$ forcing, diatom productivity and small phytoplankton productivity changes are inversely related (Figure 2b). Relative to the $E_{inh}^*(0)$ case, diatoms perform

Annual mean γ_{UV} for all PFTs

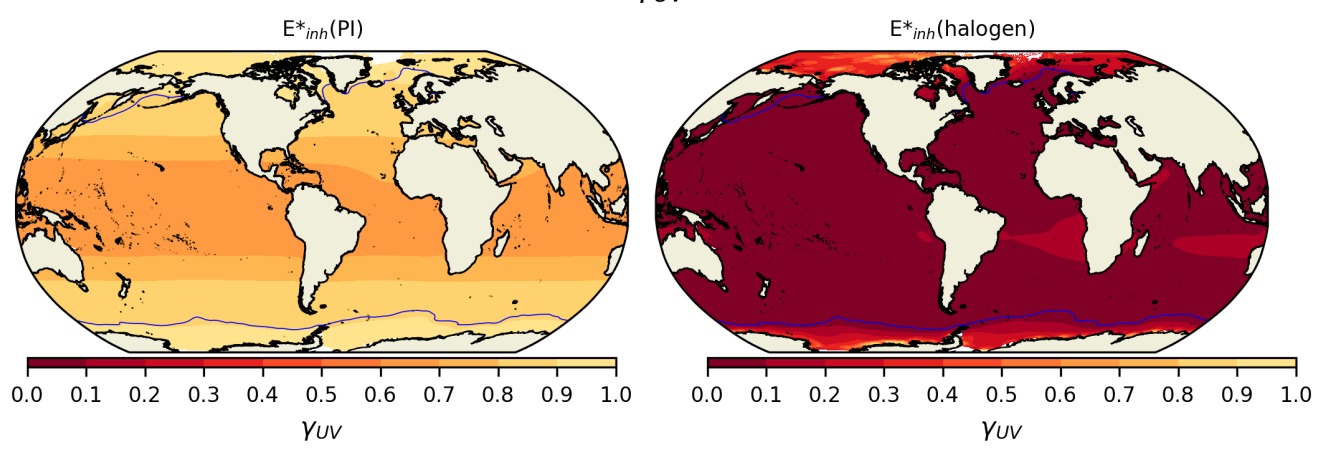


Figure 3. The spatial distribution of total average surface γ_{UV} for all PFTs under (left) E^*_{inh} (PI) and (right) E^*_{inh} (halogen) over five years of simulation, weighted by the distribution of each PFT. Maximum annual sea ice extent is indicated by the blue solid line. Lower values of γ_{UV} indicate greater plankton limitation.

better during April, November, December, and January (Figure 2b). During the month of April, small phytoplankton shift from comprising a clear majority of global phytoplankton NPP to generating nearly the same global productivity as diatoms in the E_{inh}^* (halogen) case (Figure 2b). The relative contribution of diazotrophs to global total NPP is not modified with UV radiation (Figure 2b). E_{inh}^* (halogen) forcing reduces the contribution of coccolithophore productivity to global NPP from December to February.

The relative responses of phytoplankton NPP to UV radiation across the different PFTs are driven primarily by the BWFs of the different PFTs (Figure 1) which generate E_{inh}^* . Generally, lower latitudes have higher damage under E_{inh}^* (PI) forcing (Figure 3). In the E_{inh}^* (halogen) simulation, small phytoplankton have the most damaging γ_{UV} . The net impact of UV radiation on phytoplankton NPP in CESM2-UVphyto is further determined by the latitude and depth at which the majority of the population of each PFT resides. For example, the highest E_{inh}^* values can be found at the lowest latitudes (Figure 3a) and small phytoplankton exist in greatest numbers at low latitudes, indicating high vulnerability relative to the other phytoplankton types. Under preindustrial levels of UV radiation (case E_{inh}^* (PI)), the spatial distribution of phytoplankton productivity for each PFT (Figure 4a) is similar to the distributions reported in Long et al. (2021) using a MARBL-3p1z configuration that resolves these functional types. Coccolithophore NPP (Figure 4a) and their CaCO₃ production (not shown) shares broad similarities to patterns reported in Krumhardt et al. (2019) using a MARBL-4p1z configuration that includes coccolithophores. The addition of a second zooplankton class reduces excessive CaCO₃ production in large blooms present in the MARBL-4p1z configuration. Relative to a case with no UV radiation ($E_{inh}^*(0)$), small phytoplankton and diazotrophs experience declines in NPP in the tropical and subtropical regions, where they have higher biomass under normal conditions relative to other regions; small phytoplankton have increased NPP in the subpolar regions, at the expense of coccolithophore NPP, indicating that decreased

360

365

(a) Annual mean NPP under $E *_{inh}(PI)$

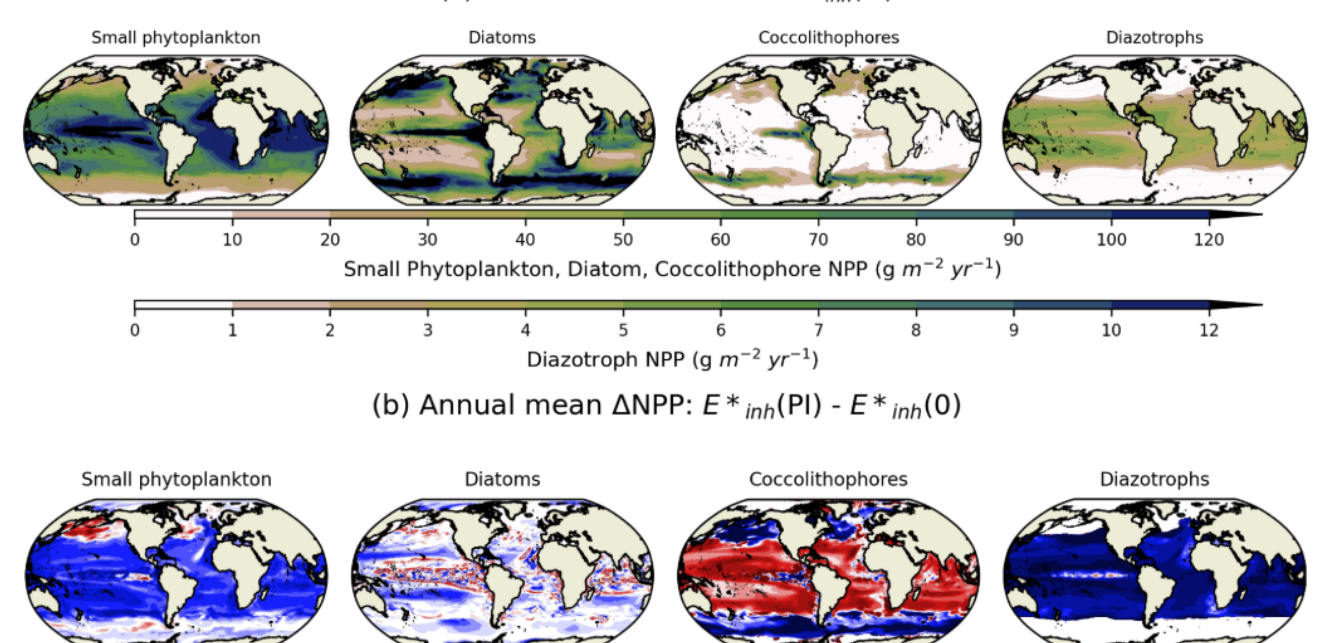


Figure 4. (a) The spatial distribution of 5 year annual mean productivity vertically integrated over the top 150 m (g C m⁻² yr⁻¹) in the $E*_{inh}(PI)$ simulation for small phytoplankton, diatoms, coccolithophores, and diazotrophs. (b) Percent change in annual mean NPP for $E*_{inh}(PI) - E*_{inh}(0)$

Δ NPP (% change)

10

12

16

20

.

-16

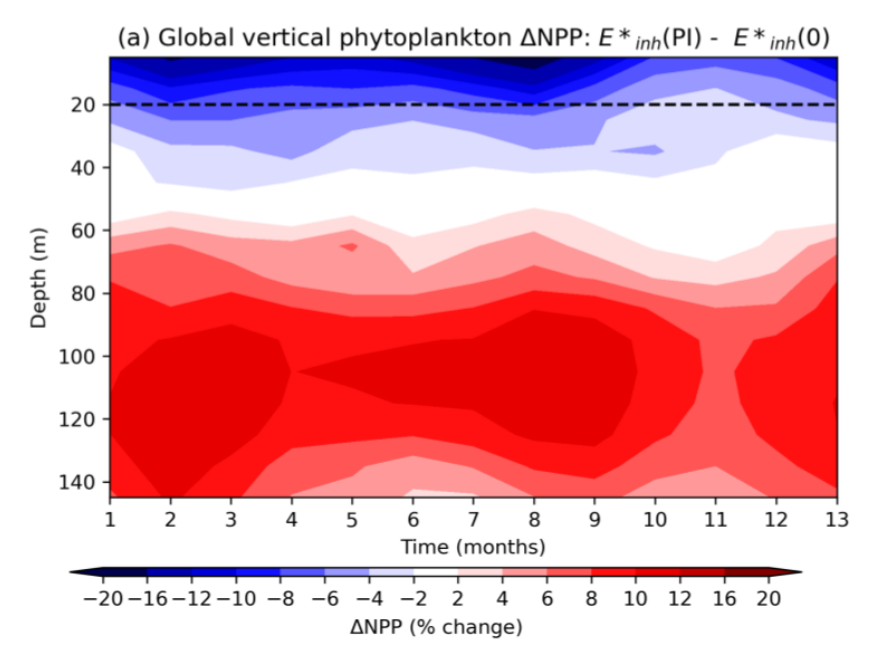
375

380

-10

fitness of coccolithophores in the regions where they are most abundant creates habitat for small phytoplankton productivity under UV stress (Figure 4b). Coccolithophores are far more productive in the subtropics and tropics where small phytoplankton experience up to a 15% decline in productivity compared to the simulation with $E_{inh}^*(0)$ forcing.

While UV inhibition in the top \sim 35 m of the ocean drives a global decline of phytoplankton NPP with increasing UV radiation, an increase in productivity below this depth compensates for the near-surface decline in many regions. Figure 5 shows the UV-radiation driven change in global NPP at each depth level and month over the course of 5 years under $E^*_{inh}(PI)$ compared to $E^*_{inh}(0)$, expressed as a percent change. The top layer of the ocean (mid-point of 5 m depth) experiences up to a 15% reduction in NPP, compared to only a 2-4% decrease in NPP in the model's 4^{th} layer (mid-point of 35 m) (Figure 5). Deeper levels of the ocean experience a surge in productivity in response to increasing UV radiation (e.g., an 8% increase in NPP at 95 m). UV-driven decreases in phytoplankton biomass (not shown; similar to NPP) in the top layers allow for an increase in PAR at deeper layers due to a reduction in phytoplankton shading. UV-driven decreases in nutrient uptake in the



(b) Annual mean phytoplankton $\triangle NPP$: $E *_{inh}(PI) - E *_{inh}(0x PI)$

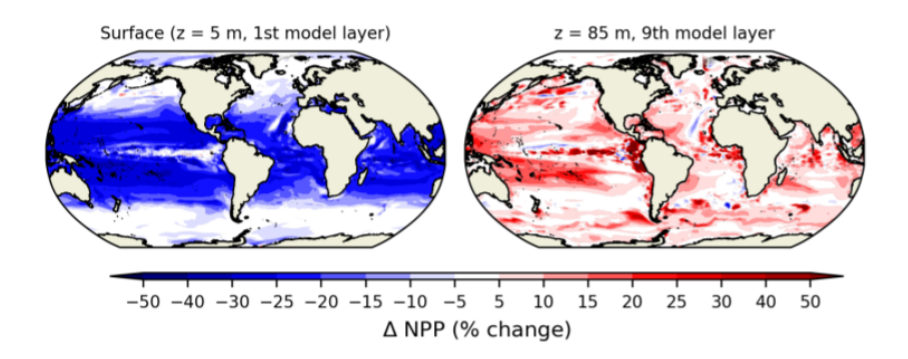


Figure 5. (a) UV-driven change in global-mean NPP (g C yr^{-1} m^{-1}) as a function of depth, calculated as the NPP from the $E*_{inh}(PI)$ simulation minus the NPP from the $E*_{inh}(0x PI)$ simulation over 5 years. The dashed black line represents the average depth where UV-B radiation attenuates to 1% of its surface value. (b) Map of annual mean NPP percent change from the $E*_{inh}(PI)$ simulation minus the NPP from the $E*_{inh}(0x PI)$ simulation at (left) 5m and (right) 85 m depth over 5 years of simulation.

surface layers (not shown) relieves nutrient limitation throughout the mixed layer. Coccolithophores' subsurface productivity enhancement is partly responsible for an increase in their total column productivity across the subtropics and tropics.

Certain types of coccolithophores can be uniquely sensitive to UV radiation when CO_2 is elevated, which is represented in CESM2-UVphyto with PIC/POC scaling. UV inhibition of coccolithophore growth rates are scaled by the inverse of PIC/POC^(1/6) (see Section 2.4). As atmospheric CO_2 and thus the aqueous CO_2 concentration increases, the PIC/POC dis-



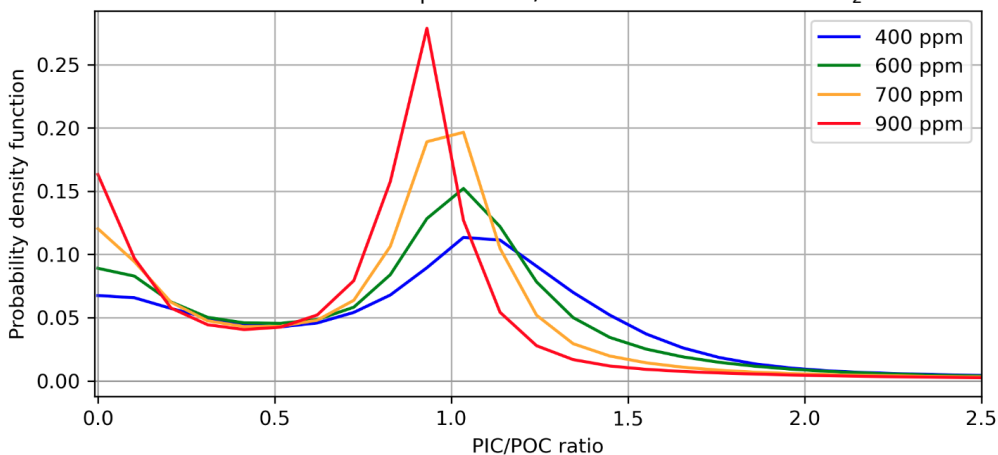


Figure 6. The probability density function for annual mean PIC/POC, weighted by coccolithophore biomass, for a 10-year spin-up where CO₂ is 400 ppm, 600 ppm, 700 ppm, and 900 ppm.

tribution of simulated coccolithophores shifts (Figure 6). PIC/POC shows a bimodal distribution, with peak densities near 0 and 1.0 (Figure 6). With increasing CO_2 , a greater proportion of thin-shelled coccolithophores are characterized as "naked" (PIC/POC<0.05), while the thick-shelled coccolithophores (PIC/POC \approx 1.0) see a shift in their distribution to lower PIC/POC values, akin to shell thinning (Krumhardt et al., 2019).

390

395

400

405

Globally integrated coccolithophore NPP, while not a major driver of total phytoplankton NPP in the model (Figure 2b), is nevertheless influenced by UV radiation and CO_2 concentration. Under atmospheric CO_2 concentrations of 284 ppm, global coccolithophore NPP is 4.5 Pg C yr⁻¹. Under $E_{inh}^*(PI)$ and atmospheric CO_2 of 284 ppm, global coccolithophore NPP increases by 3.6% to 4.6 Pg C yr⁻¹ (Figure 2b, Figure 7). Under atmospheric CO_2 concentrations of 284 ppm, increasing UV radiation produces a 4% decline in globally integrated coccolithophore NPP in the surface ocean, but an overall increase in upper-ocean integrated global coccolithophore NPP (Figure 7), due to enhanced subsurface productivity. Coccolithophore NPP shows increasing sensitivity to UV radiation under higher atmospheric CO_2 concentrations (Figure 7). Our two simulations with atmospheric CO_2 concentrations of 700 ppm and 900 pm generate 11% and 13% lower global surface coccolithophore productivity, respectively, under pre-industrial levels of UV radiation compared to no UV radiation (Figure 7).

We assess the spatial heterogeneity in the phytoplankton NPP response to UV radiation under different atmospheric CO₂ concentrations using the core biomes defined by Fay et al. (2014). In general, coccolithophores tend to be most negatively impacted by UV radiation in the seasonally ice-covered and subpolar biomes of the north Pacific, north Atlantic, and Southern Ocean (Figure 8a). The abundance of coccolithophores in these biomes, coupled with their relatively low PIC/POC values mean that coccolithophores are responsive to UV radiation increases here even under low levels of atmospheric CO₂. In contrast, coccolithophore NPP increases in response to UV radiation in subtropical and tropical biomes under low levels of atmospheric CO₂, as small phytoplankton productivity declines (Figure 8a). Under atmospheric CO₂ of 900 ppm, most biomes show a loss

Effect of E*_{inh}(PI) on global coccolithophore NPP as a function of CO₂:

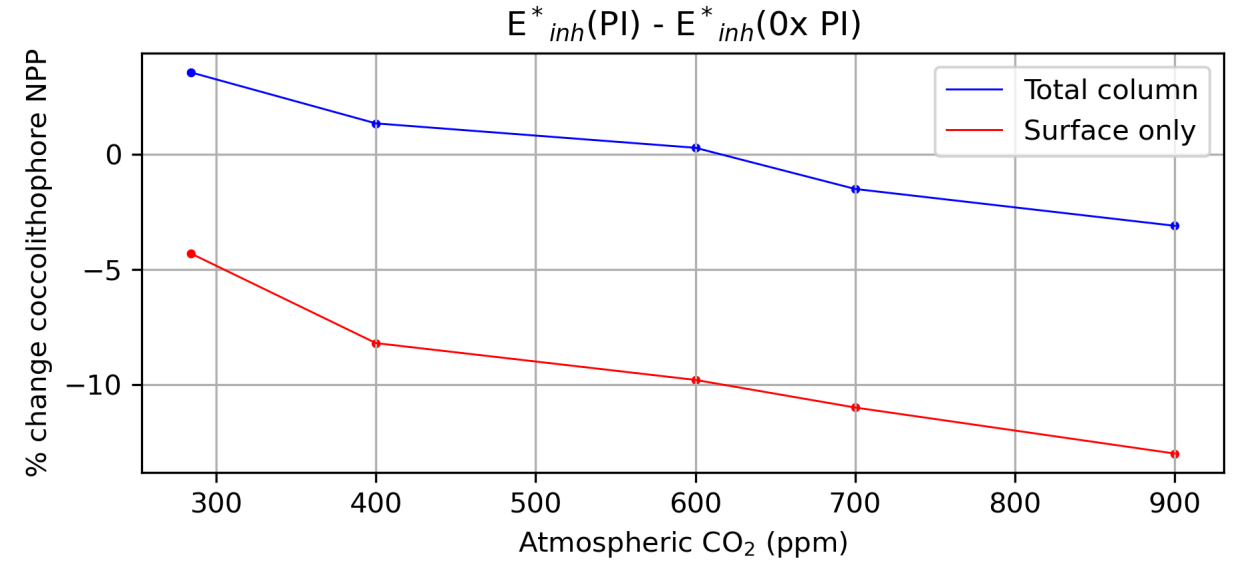


Figure 7. Annual mean coccolithophore net primary productivity percent change under simulation with $E*_{inh}(PI)$ forcing compared to $E*_{inh}(0x PI)$ with varying atmospheric CO_2 .

in coccolithophore productivity with increasing UV radiation (Figure 8b). Figure 8c illustrates the role of increasing CO₂ on coccolithophore NPP sensitivity to UV radiation in the Southern Ocean Subtropical Seasonally Stratified biome (SO-STSS; biome 15). Here, coccolithophore NPP reductions under UV radiation are enhanced by 5-30% when atmospheric CO₂ increases from 284 ppm to 900 ppm, with the largest enhancements in April, November and December (Figure 8c).

4 Discussion

410

420

Changes in phytoplankton NPP are simulated in response to UV radiation, with variations that occur as a function of latitude, depth, temperature, nutrient availability, and other phytoplankton characteristics. Globally integrated small phytoplankton NPP is particularly impacted by UV radiation due to high rates of productivity at low latitudes and high inhibition relative to the other biological weighting functions. Small phytoplankton benefit from UV radiation increases in the subpolar North Pacific, and spatial variability in the response to UV radiation is evident across phytoplankton functional types. At pre-industrial levels of atmospheric CO₂, coccolithophore shell thinning is a non-factor except in some high latitude regions. In fact, because of coccolithophore resilience to UV radiation incorporated into the BWF used to compute UV inhibition, coccolithophores benefit at the expense of small phytoplankton across the entire mixed layer.

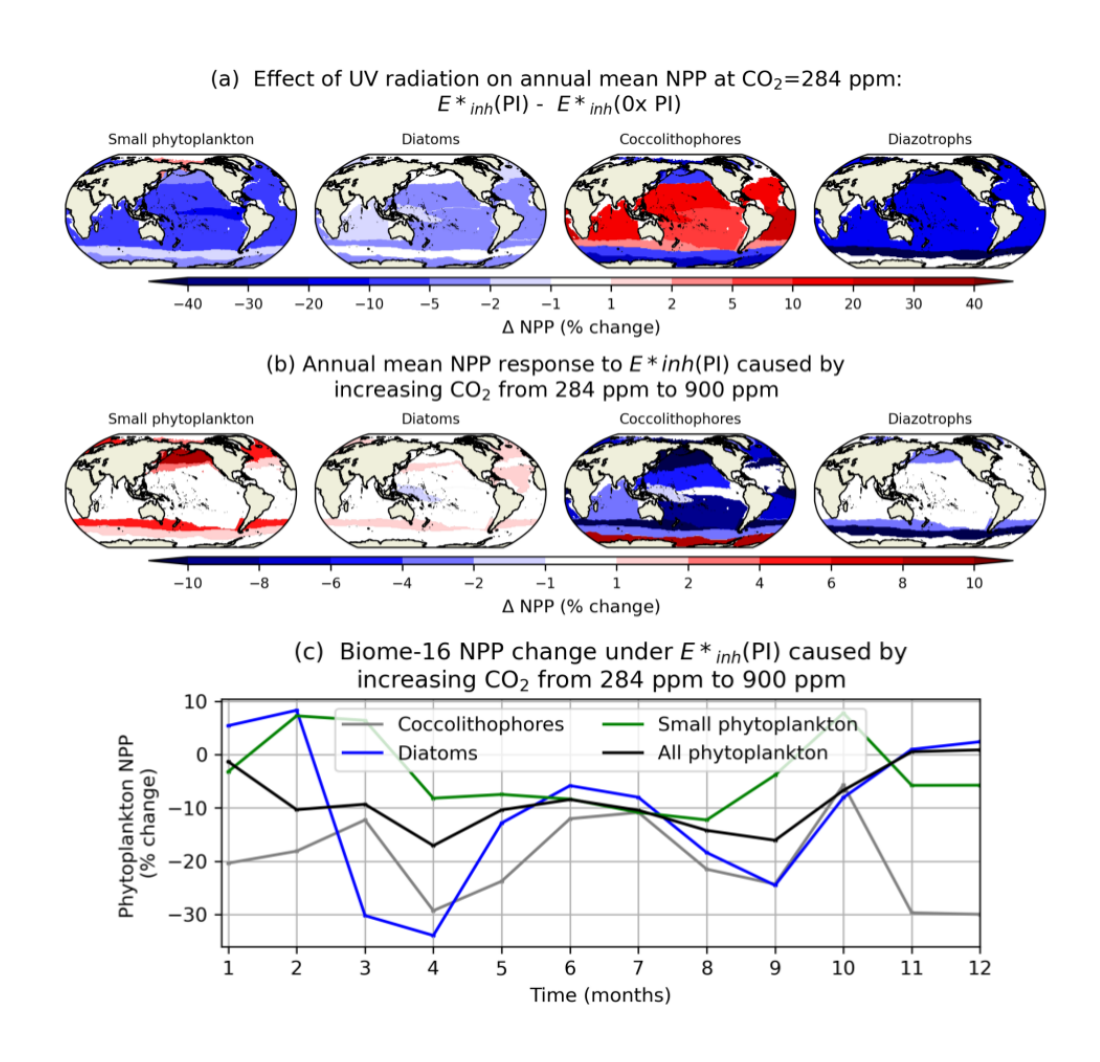


Figure 8. (a) Annual mean percent change in upper-ocean integrated NPP across 17 biomes under $E_{inh}^*(PI) - E_{inh}^*(0X PI)$ and with $CO_2=284$ ppm. (b) Annual difference in percent change in NPP across 17 biomes under $E_{inh}^*(PI) - E_{inh}^*(0X PI)$ attributable to increasing CO_2 from 284 ppm to 900 ppm. (c) Different in monthly phytoplankton NPP for biome 15 (Southern Ocean Subtropical Seasonally Stratified) under $E_{inh}^*(PI) - E_{inh}^*(0X PI)$ attributable to increasing CO_2 from 284 ppm to 900 ppm.

The simulations presented here use pre-industrial boundary conditions and therefore exhibit slightly less UV radiation compared to similar simulations with present day ozone distributions. The phytoplankton response in the surface ocean is likely to be enhanced in the present day compared to the pre-industrial, but would still be less than the E_{inh}^* (halogen) simulation.

425

430

435

440

445

Observational studies of regional phytoplankton productivity changes in response to ambient UV radiation range from a 0.15% annual mean reduction in NPP south of the Polar Front in the Southern Ocean (Helbling et al., 1992) to a 4% to 7% reduction in NPP during austral spring across the Southern Ocean (Prézelin et al., 1994). Smith et al. (1992) found a 3% reduction in a population of *Phaeocystis* when exposed to typical UV radiation levels, equivalent to an ozone layer with a thickness of 350 dobson units (DU), which is higher than typical values simulated under E_{inh}^* (PI) (310 DU). In the E_{inh}^* (PI) simulation, some parts of the Southern Ocean experience up to a 15% decline in NPP, adjacent to areas with an equally large increase in productivity. On average the Southern Ocean experiences a 5% to 10% decline in annual mean productivity, driven by coccolithophore decline. Small phytoplankton, the PFT most closely resembling *Phaeocystis*, experience a 3% decline at most and benefit in areas with the greatest coccolithophore loss. This is on the lower end of the Smith et al. (1992)'s findings for *Phaeocystis* but precise validation is made difficult by the large uncertainty range. The primary difficulty lies in the lack of information regarding how phytoplankton across most of the world, which did not experience an ozone hole, would be impacted by increased UV radiation.

The development of CESM2-UVphyto is challenged by our understanding of how phytoplankton respond to increased UV radiation. The calculation of UV damage (E_{inh}^*) in CESM2-UVphyto is specific to each phytoplankton type, yet only a small number of laboratory studies report BWFs for the modeled PFTs. We caution that the model is somewhat sensitive to the exact BWF employed; the PFTs in MARBL represent many different types of phytoplankton while the BWFs are based on laboratory experiments with a single species. Furthermore, there is a limited temperature range over which BWFs are reported, typically between 20° C and 26° C, which can affect the modeled representation of UV inhibition at cold temperatures. No BWFs are available for diazotrophs and there exist different BWFs for coccolithophores in the literature. BWFs are typically determined from short-term growth inhibition, which may not reflect the effects of direct damage to DNA over longer timescales. Over longer simulations under UV radiation, inaccuracy in the BWFs may lead to drifts in nitrogen, alkalinity, calcium carbonate, etc. compared to the observed ocean. Further research developing BWFs with laboratory studies that are more tailored to the species used to represent each PFT in MARBL and across larger temperature ranges would narrow uncertainties in simulating UV inhibition of photosynthesis. CESM2-UVphyto can be used to quickly assess how new laboratory-derived BWFs for different phytoplankton species would affect phytoplankton biomass, carbon export, marine organisms at upper trophic levels that are supported by phytoplankton.

CESM2-UVphyto horizontal and vertical resolution may also play a role in the fidelity of our simulations. At 1 degree nominal horizontal resolution, mesoscale features and some coastal processes are not represented, an absence that potentially impacts the timing and spatial scale of phytoplankton blooms. Scaling UV radiation penetration into the ocean based on wave properties was not possible in CESM2-UVphyto, but higher resolution modeling with parameterizations accounting for the scattering of UV when encountering waves and whitecaps could improve the simulation of UV radiation penetration into the ocean. We expect regions with significant wave activity to likely experience an overestimate in UV inhibition, while calmer,

subtropical waters likely experience an underestimate in our model simulations. Finally, because UV attenuates so quickly with depth, the available 10 m vertical spacing in CESM2-UVphyto may produce small inaccuracies in UV inhibition of photosynthesis that can affect the vertical profile of phytoplankton and as a result, the shading of PAR and PAR amounts deeper in the water column. Implementation of UV inhibition in a model with higher vertical resolution would likely resolve these processes with greater accuracy. Zooplankton biomass is not considered in shading equations for PAR or UV radiation, potentially leading to small errors in radiation propagation. The absence of chlorophyll in zooplankton minimize its effectiveness at intercepting PAR, but its effects on UV radiation is less clear.

5 Conclusions

460

465

470

480

We have implemented inhibition of photosynthesis from UV radiation for four different types of phytoplankton in the versatile ocean biogeochemistry model MARBL, which can be incorporated into a number of global climate models. The implementation requires the computation of photosynthetic UV damage using biological weighting functions integrated over the wavelengths of UV radiation within the atmospheric model. We explored global E_{inh}^* values ranging from a healthy, pre-industrial stratosphere to a very depleted stratosphere to understand the performance of our modifications at extremes.

CESM2-UVphyto is the first fully coupled Earth system model to calculate and consider UV inhibition of photosynthesis among phytoplankton. Increased UV radiation from the ozone hole likely impacted Southern Ocean phytoplankton, but only simple models have been used to quantify this response. UV radiation may have shaped the recovery of ecosystems during the extinction event at the K-Pg boundary, but simulations of this event have not typically included the role of increased UV radiation after an asteroid impact. CESM2-UVphyto is capable of simulating the emissions from an asteroid impact and the hypothesized pulse of UV radiation afterwards. Simulating the impact of a pulse of UV radiation and its role towards an extinction event in an Earth system model is one example of a use case that can help inform interpretations of proxy records of marine organisms in the years afterwards. Furthermore, quantifying mechanisms of past extinction provides context for ongoing anthropogenic climate change which may involve enhanced UV inhibition in increasingly stratified ocean layers. Other stratospheric aerosol injection events such as volcanic eruptions, large-scale wildfires, geoengineering, or even nuclear war may pose further risks to the stratospheric ozone layer. CESM2-UVphyto provides a modeling tool for quantifying ocean ecosystem impacts of these events.

Code and data availability.

The code modifications to the CESM and Jupyter notebook entitled manuscript_figures.ipynb to generate all figures are stored on Zenodo at DOI: 10.5281/zenodo.14025743. The data used to produce figures in the main text and supplemental is archived on Zenodo at DOI: 10.5281/zenodo.11127431.

485 Author contributions.

NL conceptualized the study. CB added TUV to the atmospheric model. LG, JC, and NL determined biological weighting functions for use in MARBL. JC implemented biological weighting functions into TUV. JC designed and implemented UV inhibition in MARBL with assistance from ML. KK provided experimental 4p2z version of MARBL. JC ran the model simulations. JC analyzed simulation results and prepared the manuscript. JC, et al., assisted in preparing and reviewing the manuscript.

Competing interests.

We declare no competing interests.

Acknowledgements. Model simulations were performed on the NSF National Center for Atmospheric Research Cheyenne and Derecho supercomputers. This material is based upon work supported by the National Center for Atmospheric Research, which is a major facility sponsored by the National Science Foundation under Cooperative Agreement No. 1852977. Funding for work was provided by the National Science Foundation FRES #2021686. Funding for work was also provided by the Future of Life Institute.

References

- Aguirre, L. E., Ouyang, L., Elfwing, A., Hedblom, M., Wulff, A., and Inganäs, O.: Diatom frustules protect DNA from ultraviolet light, Scientific Reports, 8, 5138, https://doi.org/10.1038/s41598-018-21810-2, publisher: Nature Publishing Group, 2018.
- Alvarez, L. W., Alvarez, W., Asaro, F., and Michel, H. V.: Extraterrestrial Cause for the Cretaceous-Tertiary Extinction, Science, 208, 1095–1108, https://doi.org/10.1126/science.208.4448.1095, 1980.
 - Arrigo, K. R.: Impact of ozone depletion on phytoplankton growth in the Southern Ocean: large-scale spatial and temporal variability, 114, 1–12, http://www.jstor.org/stable/24849671, 1994.
- Bardeen, C. G., Garcia, R. R., Toon, O. B., and Conley, A. J.: On transient climate change at the Cretaceous-Paleogene boundary due to atmospheric soot injections, Proceedings of the National Academy of Sciences, 114, E7415, https://doi.org/10.1073/pnas.1708980114, 2017.
 - Bardeen, C. G., Kinnison, D. E., Toon, O. B., Mills, M. J., Vitt, F., Xia, L., Jägermeyr, J., Lovenduski, N. S., Scherrer, K. J. N., Clyne, M., and Robock, A.: Extreme Ozone Loss Following Nuclear War Results in Enhanced Surface Ultraviolet Radiation, 126, e2021JD035079, https://doi.org/10.1029/2021JD035079, 2021.
- Behrenfeld, M. J. and Falkowski, P. G.: Photosynthetic rates derived from satellite-based chlorophyll concentration, Limnol. and Ocean., 42, 1–20, 1997.
 - Behrenfeld, M. J., O'Malley, R. T., Siegel, D. A., McClain, C. R., Sarmiento, J. L., Feldman, G. C., Milligan, A. J., Falkowski, P. G., Letelier, R. M., and Boss, E. S.: Climate-driven trends in contemporary ocean productivity, Nature, 444, 752–755, http://dx.doi.org/10. 1038/nature05317, 2006.
- Cai, X., Hutchins, D. A., Fu, F., and Gao, K.: Effects of ultraviolet radiation on photosynthetic performance and N₂ fixation in *Trichodesmium* erythraeum IMS 101, Biogeosciences, 14, 4455–4466, https://doi.org/10.5194/bg-14-4455-2017, publisher: Copernicus GmbH, 2017.
 - Coupe, J., Stevenson, S., Lovenduski, N. S., Rohr, T., Harrison, C. S., Robock, A., Olivarez, H., Bardeen, C. G., and Toon, O. B.: Nuclear Niño response observed in simulations of nuclear war scenarios, 2, 18, https://doi.org/10.1038/s43247-020-00088-1, 2021.
- Cullen, J. J., Neale, P. J., and Lesser, M. P.: Biological Weighting Function for the Inhibition of Phytoplankton Photosynthesis by Ultraviolet Radiation, Science, 258, 646–650, https://doi.org/10.1126/science.258.5082.646, 1992.
 - Danabasoglu, G., Lamarque, J. F., Bacmeister, J., Bailey, D. A., DuVivier, A. K., Edwards, J., Emmons, L. K., Fasullo, J., Garcia, R., Gettelman, A., Hannay, C., Holland, M. M., Large, W. G., Lauritzen, P. H., Lawrence, D. M., Lenaerts, J. T. M., Lindsay, K., Lipscomb, W. H., Mills, M. J., Neale, R., Oleson, K. W., Otto-Bliesner, B., Phillips, A. S., Sacks, W., Tilmes, S., van Kampenhout, L., Vertenstein, M., Bertini, A., Dennis, J., Deser, C., Fischer, C., Fox-Kemper, B., Kay, J. E., Kinnison, D., Kushner, P. J., Larson, V. E., Long, M. C.,
- Mickelson, S., Moore, J. K., Nienhouse, E., Polvani, L., Rasch, P. J., and Strand, W. G.: The Community Earth System Model Version 2 (CESM2), 12, e2019MS001916, https://doi.org/10.1029/2019MS001916, 2020.
 - Evan, S., Brioude, J., Rosenlof, K. H., Gao, R.-S., Portmann, R. W., Zhu, Y., Volkamer, R., Lee, C. F., Metzger, J.-M., Lamy, K., Walter, P., Alvarez, S. L., Flynn, J. H., Asher, E., Todt, M., Davis, S. M., Thornberry, T., Vömel, H., Wienhold, F. G., Stauffer, R. M., Millán, L., Santee, M. L., Froidevaux, L., and Read, W. G.: Rapid ozone depletion after humidification of the stratosphere by the Hunga Tonga
- Eruption, Science, 382, eadg2551, https://doi.org/10.1126/science.adg2551, publisher: American Association for the Advancement of Science, 2023.
 - Falkowski, P.: Ocean Science: The power of plankton, Nature, 483, S17–S20, https://doi.org/10.1038/483S17a, 2012.

- Fay, A. R., McKinley, G. A., and Lovenduski, N. S.: Southern Ocean carbon trends: Sensitivity to methods, Geophys. Res. Lett., 41, 6833–6840. https://doi.org/10.1002/2014GL061324. 2014.
- Fox, L., Stukins, S., Hill, T., and Miller, C. G.: Quantifying the Effect of Anthropogenic Climate Change on Calcifying Plankton, Scientific Reports, 10, 1620, https://doi.org/10.1038/s41598-020-58501-w, number: 1 Publisher: Nature Publishing Group, 2020.
 - Gao, K., Beardall, J., Häder, D.-P., Hall-Spencer, J. M., Gao, G., and Hutchins, D. A.: Effects of Ocean Acidification on Marine Photosynthetic Organisms Under the Concurrent Influences of Warming, UV Radiation, and Deoxygenation, Frontiers in Marine Science, 6, https://www.frontiersin.org/articles/10.3389/fmars.2019.00322, 2019.
- Garcia, R. R., Kinnison, D. E., and Marsh, D. R.: "World avoided" simulations with the Whole Atmosphere Community Climate Model, Journal of Geophysical Research: Atmospheres, 117, https://doi.org/10.1029/2012JD018430, _eprint: https://onlinelibrary.wiley.com/doi/pdf/10.1029/2012JD018430, 2012.
 - Geider, R. J., MacIntyre, H. L., and Kana, T. M.: A dynamic regulatory model of phytoplanktonic acclimation to light, nutrients, and temperature, 43, 679–694, https://doi.org/10.4319/lo.1998.43.4.0679, 1998.
- Guan, W. and Gao, K.: Impacts of UV radiation on photosynthesis and growth of the coccolithophore Emiliania huxleyi (Haptophyceae), Environmental and Experimental Botany, 67, 502–508, https://doi.org/10.1016/j.envexpbot.2009.08.003, 2010.
 - Harrison, C. S., Rohr, T., DuVivier, A., Maroon, E. A., Bachman, S., Bardeen, C. G., Coupe, J., Garza, V., Heneghan, R., Lovenduski, N. S., Neubauer, P., Rangel, V., Robock, A., Scherrer, K., Stevenson, S., and Toon, O. B.: A New Ocean State After Nuclear War, AGU Advances, 3, e2021AV000610, https://doi.org/https://doi.org/10.1029/2021AV000610, 2022.
- Helbling, E. W., Villafañe, V., Ferrario, M., and Holm-Hansen, O.: Impact of natural ultraviolet radiation on rates of photosynthesis and on specific marine phytoplankton species, Marine Ecology Progress Series, 80, 89–100, http://www.jstor.org/stable/24826547, 1992.
 - Henehan, M. J., Ridgwell, A., Thomas, E., Zhang, S., Alegret, L., Schmidt, D. N., Rae, J. W. B., Witts, J. D., Landman, N. H., Greene, S. E., Huber, B. T., Super, J. R., Planavsky, N. J., and Hull, P. M.: Rapid ocean acidification and protracted Earth system recovery followed the end-Cretaceous Chicxulub impact, Proc. Nat. Acad. Sci. USA, 201905989, https://doi.org/10.1073/pnas.1905989116, 2019.
- Hunke, E. C., Lipscomb, W. H., Turner, A. K., Jeffery, N., and Elliott, S. M.: CICE: the Los Alamos sea ice model documentation and software user's manual 1568 version 5.1, Los Alamos Natl. Lab. Tech. Report, 2015.
 - Iacono, M. J., Mlawer, E. J., Clough, S. A., and Morcrette, J.-J.: Impact of an improved longwave radiation model, RRTM, on the energy budget and thermodynamic properties of the NCAR community climate model, CCM3, 105, 14873–14890, https://doi.org/10.1029/2000JD900091, 2000.
- Jablonski, D., Chaloner, W. G., Lawton, J. H., and May, R. M.: Extinctions in the fossil record, Philosophical Transactions of the Royal Society of London. Series B: Biological Sciences, 344, 11–17, https://doi.org/10.1098/rstb.1994.0045, publisher: Royal Society, 1997.
 - Krumhardt, K., Long, M. C., Petrik, C. M., Levy, M., Castruccio, F., Lindsay, K., Romashkov, L., Deppenmeier, A.-L., Denéchère, R., Chen, Z., Landrum, L., Danabasoglu, G., and Chang, P.: From nutrients to fish: Impacts of mesoscale processes in a global CESM-FEISTY eddying ocean model framework, https://eartharxiv.org/repository/view/6673/, publisher: EarthArXiv, 2024.
- Krumhardt, K. M., Lovenduski, N. S., Long, M. C., and Lindsay, K.: Avoidable impacts of ocean warming on marine primary production: Insights from the CESM ensembles, 31, 114–133, https://doi.org/10.1002/2016GB005528, 2017.
 - Krumhardt, K. M., Lovenduski, N. S., Long, M. C., Levy, M., Lindsay, K., Moore, J. K., and Nissen, C.: Coccolithophore growth and calcification in an acidified ocean: Insights from Community Earth System Model simulations, 11, 1418–1437, https://doi.org/10.1029/2018MS001483, 2019.

- Lawrence, D. M., Fisher, R. A., Koven, C. D., Oleson, K. W., Swenson, S. C., Bonan, G., Collier, N., Ghimire, B., van Kampenhout, L., Kennedy, D., Kluzek, E., Lawrence, P. J., Li, F., Li, H., Lombardozzi, D., Riley, W. J., Sacks, W. J., Shi, M., Vertenstein, M., Wieder, W. R., Xu, C., Ali, A. A., Badger, A. M., Bisht, G., van den Broeke, M., Brunke, M. A., Burns, S. P., Buzan, J., Clark, M., Craig, A., Dahlin, K., Drewniak, B., Fisher, J. B., Flanner, M., Fox, A. M., Gentine, P., Hoffman, F., Keppel-Aleks, G., Knox, R., Kumar, S., Lenaerts, J., Leung, L. R., Lipscomb, W. H., Lu, Y., Pandey, A., Pelletier, J. D., Perket, J., Randerson, J. T., Ricciuto, D. M., Sanderson, B. M., Slater,
- A., Subin, Z. M., Tang, J., Thomas, R. Q., Val Martin, M., and Zeng, X.: The Community Land Model Version 5: Description of New Features, Benchmarking, and Impact of Forcing Uncertainty, 11, 4245–4287, https://doi.org/10.1029/2018MS001583, 2019.
 - Lesser, M. P.: Effects of ultraviolet radiation on productivity and nitrogen fixation in the Cyanobacterium, Anabaena sp. (Newton's strain), Hydrobiologia, 598, 1–9, https://doi.org/10.1007/s10750-007-9126-x, 2008.
- Li, G., Cheng, L., Zhu, J., Trenberth, K. E., Mann, M. E., and Abraham, J. P.: Increasing ocean stratification over the past half-century, https://doi.org/10.1038/s41558-020-00918-2, 2020.
 - Long, M. C., Lindsay, K., and Holland, M. M.: Modeling photosynthesis in sea ice-covered waters, 7, 1189–1206, https://doi.org/10.1002/2015MS000436, 2015.
 - Long, M. C., Moore, J. K., Lindsay, K., Levy, M., Doney, S. C., Luo, J. Y., Krumhardt, K. M., Letscher, R. T., Grover, M., and Sylvester, Z. T.: Simulations With the Marine Biogeochemistry Library (MARBL), 13, e2021MS002647, https://doi.org/10.1029/2021MS002647, 2021.

- Lorenzo, M. R., Neale, P. J., Sobrino, C., León, P., Vázquez, V., Bresnan, E., and Segovia, M.: Effects of elevated CO2 on growth, calcification, and spectral dependence of photoinhibition in the coccolithophore Emiliania huxleyi (Prymnesiophyceae)1, Journal of Phycology, 55, 775–788, https://doi.org/10.1111/jpy.12885, _eprint: https://onlinelibrary.wiley.com/doi/pdf/10.1111/jpy.12885, 2019.
- Lovenduski, N. S., Harrison, C. S., Olivarez, H., Bardeen, C. G., Toon, O. B., Coupe, J., Robock, A., Rohr, T., and Stevenson, S.: The Potential

 Impact of Nuclear Conflict on Ocean Acidification, Geophys. Res. Lett., 47, e2019GL086246, https://doi.org/10.1029/2019GL086246,
 2020.
 - MacMartin, D. G., Wang, W., Kravitz, B., Tilmes, S., Richter, J. H., and Mills, M. J.: Timescale for Detecting the Climate Response to Stratospheric Aerosol Geoengineering, Journal of Geophysical Research: Atmospheres, 124, 1233–1247, https://doi.org/10.1029/2018JD028906, _eprint: https://onlinelibrary.wiley.com/doi/pdf/10.1029/2018JD028906, 2019.
- Marsh, D. R., Mills, M. J., Kinnison, D. E., Lamarque, J.-F., Calvo, N., and Polvani, L. M.: Climate Change from 1850 to 2005 Simulated in CESM1(WACCM), 26, 7372–7391, https://doi.org/10.1175/JCLI-D-12-00558.1, 2013.
 - Marshall, J. E. A., Lakin, J., Troth, I., and Wallace-Johnson, S. M.: UV-B radiation was the Devonian-Carboniferous boundary terrestrial extinction kill mechanism, Science Advances, 6, eaba0768, https://doi.org/10.1126/sciadv.aba0768, 2020.
- Monteiro, F. M., Bach, L. T., Brownlee, C., Bown, P., Rickaby, R. E. M., Poulton, A. J., Tyrrell, T., Beaufort, L., Dutkiewicz, S., Gibbs, S.,
 Gutowska, M. A., Lee, R., Riebesell, U., Young, J., and Ridgwell, A.: Why marine phytoplankton calcify, Science Advances, 2, e1501822, https://doi.org/10.1126/sciadv.1501822, publisher: American Association for the Advancement of Science, 2016.
 - Neale, P. J. and Thomas, B. C.: Inhibition by ultraviolet and photosynthetically available radiation lowers model estimates of depth-integrated picophytoplankton photosynthesis: global predictions for Prochlorococcus and Synechococcus, Global Change Biology, 23, 293–306, https://doi.org/10.1111/gcb.13356, _eprint: https://onlinelibrary.wiley.com/doi/pdf/10.1111/gcb.13356, 2016.
- Neale, P. J., Banaszak, A. T., and Jarriel, C. R.: Ultraviolet Sunscreens in Gymnodinium Sanguineum (dinophyceae): Mycosporine-Like Amino Acids Protect Against Inhibition of Photosynthesis, Journal of Phycology, 34, 928–938, https://doi.org/10.1046/j.1529-8817.1998.340928.x, _eprint: https://onlinelibrary.wiley.com/doi/pdf/10.1046/j.1529-8817.1998.340928.x, 1998.

- Neale, P. J., Pritchard, A. L., and Ihnacik, R.: UV effects on the primary productivity of picophytoplankton: biological weighting functions and exposure response curves of *Synechococcus*, Biogeosciences, 11, 2883–2895, https://doi.org/10.5194/bg-11-2883-2014, publisher:

 Copernicus GmbH, 2014.
 - Østerstrøm, F. F., Klobas, J. E., Kennedy, R. P., Cadoux, A., and Wilmouth, D. M.: Sensitivity of stratospheric ozone to the latitude, season, and halogen content of a contemporary explosive volcanic eruption, Scientific Reports, 13, 6457, https://doi.org/10.1038/s41598-023-32574-9, number: 1 Publisher: Nature Publishing Group, 2023.
- Pierazzo, E., Garcia, R. R., Kinnison, D. E., Marsh, D. R., Lee-Taylor, J., and Crutzen, P. J.: Ozone perturbation from medium-size asteroid impacts in the ocean, Earth and Planetary Science Letters, 299, 263–272, https://doi.org/10.1016/j.epsl.2010.08.036, 2010.
 - Prézelin, B. B., Boucher, N. P., and Schofield, O.: Evaluation of Field Studies of UVB Radiation Effects on Antarctic Marine Primary Productivity, in: Stratospheric Ozone Depletion/UV-B Radiation in the Biosphere, edited by Biggs, R. H. and Joyner, M. E. B., pp. 181–194, Springer Berlin Heidelberg, Berlin, Heidelberg, 1994.
- Ridgwell, A., Schmidt, D. N., Turley, C., Brownlee, C., Maldonado, M. T., Tortell, P., and Young, J. R.: From laboratory manipulations to

 Earth system models: scaling calcification impacts of ocean acidification, Biogeosciences, 6, 2611–2623, https://doi.org/10.5194/bg-62611-2009, publisher: Copernicus GmbH, 2009.
 - Schulte, P., Alegret, L., Arenillas, I., Arz, J. A., Barton, P. J., Bown, P. R., Bralower, T. J., Christeson, G. L., Claeys, P., Cockell, C. S., Collins, G. S., Deutsch, A., Goldin, T. J., Goto, K., Grajales-Nishimura, J. M., Grieve, R. A. F., Gulick, S. P. S., Johnson, K. R., Kiessling, W., Koeberl, C., Kring, D. A., MacLeod, K. G., Matsui, T., Melosh, J., Montanari, A., Morgan, J. V., Neal, C. R., Nichols, D. J., Norris, R. D.,
- Pierazzo, E., Ravizza, G., Rebolledo-Vieyra, M., Reimold, W. U., Robin, E., Salge, T., Speijer, R. P., Sweet, A. R., Urrutia-Fucugauchi, J., Vajda, V., Whalen, M. T., and Willumsen, P. S.: The Chicxulub Asteroid Impact and Mass Extinction at the Cretaceous-Paleogene Boundary, Science, 327, 1214–1218, https://doi.org/10.1126/science.1177265, publisher: American Association for the Advancement of Science, 2010.
- Smit, J. and Hertogen, J.: An extraterrestrial event at the Cretaceous–Tertiary boundary, Nature, 285, 198–200, https://doi.org/10.1038/285198a0, publisher: Nature Publishing Group, 1980.
 - Smith, R. C. and Cullen, J. J.: Effects of UV radiation on phytoplankton, Reviews of Geophysics, 33, 1211–1223, https://doi.org/10.1029/95RG00801, _eprint: https://onlinelibrary.wiley.com/doi/pdf/10.1029/95RG00801, 1995.
 - Smith, R. C., Prézelin, B. B., Baker, K. S., Bidigare, R. R., Boucher, N. P., Coley, T., Karentz, D., MacIntyre, S., Matlick, H. A., Menzies, D., Ondrusek, M., Wan, Z., and Waters, K. J.: Ozone Depletion: Ultraviolet Radiation and Phytoplankton Biology in Antarctic Waters, Science, 255, 952–959, https://doi.org/10.1126/science.1546292, 1992.

635

640

- Solomon, S., Garcia, R. R., Rowland, F. S., and Wuebbles, D. J.: On the depletion of Antarctic ozone, Nature, 321, 755–758, https://doi.org/10.1038/321755a0, number: 6072 Publisher: Nature Publishing Group, 1986.
- Tabor, C. R., Bardeen, C. G., Otto-Bliesner, B. L., Garcia, R. R., and Toon, O. B.: Causes and Climatic Consequences of the Impact Winter at the Cretaceous-Paleogene Boundary, Geophysical Research Letters, 47, e60 121, https://doi.org/https://doi.org/10.1029/2019GL085572, e60121 2019GL085572, 2020.
- Taucher, J., Bach, L. T., Prowe, A. E. F., Boxhammer, T., Kvale, K., and Riebesell, U.: Enhanced silica export in a future ocean triggers global diatom decline, Nature, 605, 696–700, https://doi.org/10.1038/s41586-022-04687-0, publisher: Nature Publishing Group, 2022.
- Tedetti, M., Sempéré, R., Vasilkov, A., Charrière, B., Nérini, D., Miller, W. L., Kawamura, K., and Raimbault, P.: High penetration of ultraviolet radiation in the south east Pacific waters, Geophysical Research Letters, 34, https://doi.org/10.1029/2007GL029823, _eprint: https://onlinelibrary.wiley.com/doi/pdf/10.1029/2007GL029823, 2007.

- Tilmes, S., MacMartin, D. G., Lenaerts, J. T. M., van Kampenhout, L., Muntjewerf, L., Xia, L., Harrison, C. S., Krumhardt, K. M., Mills, M. J., Kravitz, B., and Robock, A.: Reaching 1.5 and 2.0  °C global surface temperature targets using stratospheric aerosol geoengineering, Earth System Dynamics, 11, 579–601, https://doi.org/10.5194/esd-11-579-2020, publisher: Copernicus GmbH, 2020.
- Tilmes, S., Richter, J. H., Kravitz, B., MacMartin, D. G., Glanville, A. S., Visioni, D., Kinnison, D. E., and Müller, R.: Sensitivity of Total Column Ozone to Stratospheric Sulfur Injection Strategies, Geophysical Research Letters, 48, e2021GL094058, https://doi.org/10.1029/2021GL094058, _eprint: https://onlinelibrary.wiley.com/doi/pdf/10.1029/2021GL094058, 2021.
 - Tilmes, S., Visioni, D., Jones, A., Haywood, J., Séférian, R., Nabat, P., Boucher, O., Bednarz, E. M., and Niemeier, U.: Stratospheric ozone response to sulfate aerosol and solar dimming climate interventions based on the G6 Geoengineering Model Intercomparison Project (GeoMIP) simulations, Atmospheric Chemistry and Physics, 22, 4557–4579, https://doi.org/10.5194/acp-22-4557-2022, publisher: Copernicus GmbH, 2022.

- Toon, O. B., Bardeen, C., and Garcia, R.: Designing global climate and atmospheric chemistry simulations for 1 and 10\,km diameter asteroid impacts using the properties of ejecta from the K-Pg impact, Atmospheric Chemistry and Physics, 16, 13185–13212, https://doi.org/10.5194/acp-16-13185-2016, 2016.
- Vömel, H., Evan, S., and Tully, M.: Water vapor injection into the stratosphere by Hunga Tonga-Hunga Ha'apai, Science, 377, 1444–1447, https://doi.org/10.1126/science.abq2299, publisher: American Association for the Advancement of Science, 2022.
 - Xu, J., Bach, L. T., Schulz, K. G., Zhao, W., Gao, K., and Riebesell, U.: The role of coccoliths in protecting *Emiliania huxleyi* against stressful light and UV radiation, Biogeosciences, 13, 4637–4643, https://doi.org/10.5194/bg-13-4637-2016, 2016.
 - Zerefos, C. S. and Bais, A. F., eds.: Theoretical Estimation of Biologically Effective UV Radiation at the Earth's Surface, Springer Berlin Heidelberg, Berlin, Heidelberg, 1997.
- Zhu, Y., Portmann, R. W., Kinnison, D., Toon, O. B., Millán, L., Zhang, J., Vömel, H., Tilmes, S., Bardeen, C. G., Wang, X., Evan, S., Randel, W. J., and Rosenlof, K. H.: Stratospheric ozone depletion inside the volcanic plume shortly after the 2022 Hunga Tonga eruption, Atmospheric Chemistry and Physics, 23, 13 355–13 367, https://doi.org/10.5194/acp-23-13355-2023, publisher: Copernicus GmbH, 2023.